

Formation of the 15 Å phase as the most expanded hydrated mineral in cold subduction zone

Received: 26 June 2024

Accepted: 24 January 2025

Published online: 07 March 2025



Yoonah Bang^{1,2}, Juhyeok Kim³, Jinhyuk Choi^{1,9}, Heehyeon Sim¹, Dongzhou Zhang^{4,5}, Tae-Yeol Jeon⁶, Tae Joo Shin⁷, Hanns-Peter Liermann⁸, Kideok D. Kwon³ & Yongjae Lee¹✉

Talc, as an important class of clay minerals constituting subducting oceanic crust, has long been known to undergo interlayer expansion by ~6% to contain net ~13 wt.% water into the ‘so-called’ 10 Å phase. Although subduction fluid is mildly alkaline and includes various salts and other dissolved species, its effect on the stability of subducting minerals has not yet been considered. Here, we report that subducting talc, when exposed to alkaline salty water conditions, breaks down to form a super-hydrated 15 Å phase at ~3.0 GPa and ~350 °C, corresponding to a depth of ~90–95 km along a cold subduction geotherm. The 15 Å phase remains stable down to ~125 km depth, where it transforms into the previously known 10 Å phase. Our combined experimental and computational results show that the super-hydrated 15 Å phase contains net ~31 wt.% water through interlayer expansion by ~60%. Our work thus demonstrates mineral transformation under more realistic subduction environments, which calls for reevaluation of subduction-related geochemistry and seismicity as well as water transportation into the deep Earth.

Subduction-related water transportation from the Earth’s surface to its deep interior is a pivotal process that fuels the Earth’s evolution and dynamics^{1,2}. Current global subduction system transports ~7–10 × 10¹⁴ g/yr (or × 10⁸ Tg/Myr) of water into the mantle in the form of structurally bound water (or hydroxyls) within various hydrous mineral phases contained in subducting slabs^{3,4}. Experimental studies have established phase stabilities of major hydrous phases such as amphiboles, chlorite, serpentine, and dense hydrous magnesium silicates (DHMS), along diverse subduction thermal models^{3,5,6} where ca. 28.5% of the contemporary subduction has been categorized as cold system with a low thermal gradient of ~5–8 °C/km since ~800 Ma ago^{7–10}. The stability of hydrous minerals depends on hydro-chemical processes as well as

pressure-temperature (P-T) conditions, in most cases, resulting in liberation of structurally bound water in a range of subduction depths. The fluid chemistry along subducting slabs is then affected by exchange reactions with surrounding rocks while the fluid composition itself can cause changes in bulk rock composition, mineral assemblages, and mineral compositions under various chemical and physical conditions¹¹. Therefore, it is a necessity to consider hydro-chemical characteristics of subduction zone fluids (SZFs) with respect to reactions and stabilities of subducting minerals. Salt and gas such as NaCl and CO₂ are important components of the SZFs, together with dissolved silica, to affect the physical and chemical properties such as density, dielectric constant, and pH/alkalinity^{12–14}. Subduction occurs initially in seawater-dominated

¹Department of Earth System Sciences, Yonsei University, Seoul, Republic of Korea. ²Korea Atomic Energy Research Institute (KAERI), Daejeon, Republic of Korea. ³Department of Geology, Kangwon National University, Chuncheon, Republic of Korea. ⁴Hawaii Institute of Geophysics and Planetology, University of Hawaii at Manoa, Honolulu, HI, USA. ⁵GSECARS, University of Chicago, Chicago, IL, USA. ⁶Pohang Accelerator Laboratory, POSTECH, Pohang, Republic of Korea. ⁷Graduate School of Semiconductor Materials and Devices Engineering, Ulsan National Institute of Science and Technology (UNIST), Ulsan, Republic of Korea. ⁸Photon Sciences, Deutsches Elektronen-Synchrotron (DESY), Hamburg, Germany. ⁹Present address: Pohang Accelerator Laboratory, POSTECH, Pohang, Republic of Korea. ✉e-mail: yongjaelee@yonsei.ac.kr

fluid environment¹⁵ where the model calculated pH value is alkaline in the range of 8.08–8.33 due to bicarbonate ions $[\text{HCO}_3^-]$ ^{16,17}. As such, the pH and alkalinity of the SZFs have been suggested as important variables in high-pressure and high-temperature (HP-HT) mineralogy and mantle geochemistry^{18–21}. Recent studies employing theoretical and experimental approaches have further demonstrated that the pH of fluids in subducted crustal lithologies is moderately alkaline with the maximum changes of ΔpH up to ~ 2.3 along cold and intermediate P-T paths^{20–22}.

In our previous work, we reported that albite ($\text{NaAlSi}_3\text{O}_8$), one of the most abundant minerals in the oceanic crust, breaks down into mono-layer hydrated smectite with interlayer spacing of $\sim 12 \text{ \AA}$ ($\text{NaAl}_2(\text{Si}_3\text{Al})\text{O}_{10}(\text{OH})_2 \cdot \text{H}_2\text{O}$) and moganite (SiO_2) above $\sim 2.5 \text{ GPa}$ and 200°C under water-containing cold subduction geotherm²³. As the formation of the smectite assemblage from albite is accompanied by the release of OH^- (and Na^+) species into the region, alkaline fluids with as much as ΔpH of $2.2\text{--}2.5$ have been postulated and linked to the mildly alkaline nature of SZFs²³. This work called for the need to reevaluate the role of subducting fluid composition on the behavior of subducting minerals and their water transportation characteristics into the deep Earth. In this study, we have investigated the physicochemical properties and stability of subducting talc under controlled fluid compositions to simulate natural SZFs. As SZFs differ from pure water in terms of alkalinity, salts, dissolved silica, volatile contents, etc.^{12,20}, fluid composition-dependent stability of talc would therefore provide more realistic insights into understanding subduction-related geochemistry, mineralogy, and related seismic and magmatic processes.

Talc (ideal composition, $\text{Mg}_3\text{Si}_4\text{O}_{10}(\text{OH})_2$) is an important hydrous clay mineral in subduction-related environments since it commonly occurs as a metamorphic or hydrothermal alteration product in peridotite, basalt, and sediments constituting the oceanic lithosphere^{1,2,24–28}. In terms of atomic structural arrangement, talc belongs to the 2:1 type layered silicate minerals (trioctahedral phyllosilicates) consisting of an Mg-octahedral (O) layer sandwiched by two Si-tetrahedral (T) layers (Supplementary Fig. 1). Because the OH^- species, which account for $\sim 4.75 \text{ wt.}\%$ of the hydration, are distributed in the central O-layer toward the vacant Si-tetrahedral site (T_v -site), the resulting tri-layer units (TOT) are held together by weak van der Waals force to create cation- and water molecule-free interlayer with $\sim 9.37 \text{ \AA}$ spacing. The interlayer d_{OOL} -spacing of talc is non-expandable at ambient conditions, whereas it expands by $\sim 6\%$ to form the ‘so-called’ 10 \AA phase (ideal composition, $\text{Mg}_3\text{Si}_4\text{O}_{10}(\text{OH})_2 \cdot n\text{H}_2\text{O}$, $n = 0.65, 1.0, 2.0$) via water intercalation in the P-T range of $\sim 4\text{--}7 \text{ GPa}$ and $\sim 450\text{--}650^\circ\text{C}$ (refs. 29–33), corresponding to a $\sim 125\text{--}220 \text{ km}$ depth range in a cold subduction system. As such, the 10 \AA phase with $\sim 7.6\text{--}13.0 \text{ wt.}\%$ of water (counting both H_2O and OH) has been proposed to be one of the major water carriers, together with other DHMS phases, down to the lower mantle^{30,31}. This also led to the hypothesis that the $\text{MgO-SiO}_2\text{-H}_2\text{O}$ (MSH) system could be a crucial chemical model for understanding the Earth’s mantle by about $85\text{--}90 \text{ wt.}\%$ in terms of its bulk composition³².

In this study, we have investigated in-situ phase stability and transformation of talc up to $7.7(3) \text{ GPa}$ and $560 \pm 30^\circ\text{C}$ using a resistively-heated diamond-anvil cell (RH-DAC) combined with synchrotron X-ray powder diffraction (XRD). We have applied cold subduction thermal gradients of $\sim 5\text{--}8^\circ\text{C/km}$ (refs. 7–10), as modeled for the Kermadec and South Mariana subduction zones, and used salty and alkaline solutions that can be described in the $\text{Na}_2\text{O-CO}_2\text{-NaCl-H}_2\text{O}$ system to mimic natural subduction fluid compositions. Unlike previous results performed using pure water^{29–33}, we observed the formation of a ‘super-hydrated’ 15 \AA phase that contains ~ 8 times the amount of water in the original talc, together with magnesite, in the depth range between ~ 90 and $\sim 125 \text{ km}$. This manifests a hydration reaction, which would call for

reevaluation of the overall geochemical and geophysical models of subducting slabs and their surrounding regions.

Results

Hydration reaction of talc under modeled subduction fluids along cold subduction geotherm

In-situ HP-HT synchrotron XRD experiments were performed on talc mixed with $\text{NaHCO}_3(\text{l})$, $\text{NaCl}(\text{l})$, $\text{H}_2\text{O}(\text{l})$, and $\text{CO}_2(\text{g})$ in order to simulate diverse subduction fluid reactants in the $\text{Na}_2\text{O-CO}_2\text{-NaCl-H}_2\text{O}$ system (Fig. 1a, Supplementary Fig. 2, and Supplementary Table 1). Under alkaline salty water conditions using $\text{NaHCO}_3(\text{l})$, talc breaks down into an expanded phase with the interlayer d_{OOL} -spacing of $14.43(1) \text{ \AA}$ and magnesite (MgCO_3) above $3.0(2) \text{ GPa}$ and $350 \pm 20^\circ\text{C}$, corresponding to $\sim 90\text{--}95 \text{ km}$ depth along a cold subduction geotherm (Fig. 1b and Supplementary Fig. 2a). This phase assemblage remains stable up to $4.4(2) \text{ GPa}$ and $470 \pm 20^\circ\text{C}$, corresponding to $\sim 125 \text{ km}$ depth, by which the interlayer d_{OOL} -spacing of the expanded phase contracts gradually to $14.17(1) \text{ \AA}$ (Fig. 1b and Supplementary Table 2). Upon further increase in pressure and temperature above $5.3(3) \text{ GPa}$ and $480 \pm 20^\circ\text{C}$, corresponding to $\sim 165 \text{ km}$ depth, the expanded phase transforms to the previously known 10 \AA phase with the d_{OOL} -spacing of $10.40(1) \text{ \AA}$. The 10 \AA phase then remains stable up to $5.8(4) \text{ GPa}$ and $515 \pm 30^\circ\text{C}$, corresponding to $\sim 180 \text{ km}$ depth condition, by which its d_{OOL} -spacing contracts gradually down to $9.76(1) \text{ \AA}$. The 10 \AA phase is recovered upon pressure and temperature release down to ambient condition with d_{OOL} -spacing of $\sim 10.30(1) \text{ \AA}$. Based on the observed phase relationship of the expanded phase that forms between talc and its 10 \AA phase under increasing depth conditions, we call the expanded phase ‘super-hydrated’ 15 \AA phase that is expected to have a multi-layer hydration structure, compared to the mono-layer hydrated 10 \AA phase.

Grand canonical Monte Carlo (GCMC) simulations were conducted (see “Methods”, Fig. 2a, b) to estimate the interlayer water contents of hydrated talc phases with relative stabilities. As previous studies reported talc-like and phlogopite-like stacking modes for the 10 \AA phase^{24,34}, the two different staking modes were considered in the simulations. In the phlogopite-like stacking mode, basal oxygens of T-layers are superimposable across the interlayer (Fig. 2c), whereas the oxygens in the talc-like stacking mode are staggered across the interlayer (Fig. 2d). Based on the estimated water contents, three energy minima were identified in the interaction energy curves, mainly at d_{OOL} -spacings of $\sim 10, 12$, and 15 \AA , although the phlogopite-like model exhibited an additional minimum at 9.4 \AA (Fig. 2a). The estimated water contents of hydrated talc phases at the apparent energy minima are $\sim 9, \sim 19$, and $\sim 28 \text{ wt.}\%$ for interlayer H_2O (or $\sim 13, \sim 23$, and $\sim 31 \text{ wt.}\%$ including the intralayer OH species), respectively (Fig. 2b).

Molecular dynamics (MD) simulations were performed on those hydrated talc phases with relative stabilities. As expected, the hydroxyls in the central O-layer are modeled to be oriented toward the T_v -site in the basal T-layer. In the 10 \AA phase, these hydroxyls form hydrogen-bonds by $\sim 2.5 \text{ \AA}$ with intercalated H_2O molecules in the interlayer while the dipole moments of the interlayer H_2O are oriented almost vertically to the basal T-layer (Fig. 2e, f). Such an H_2O bound to the T_v -site appears to be a unique feature in the water structure of hydrated talc phases formed at high pressure. In the phlogopite-like 10 \AA phase (precisely $d_{\text{OOL}} = 9.4 \text{ \AA}$), interlayer H_2O resides between a pair of upper and lower T_v -sites, forming a hydrogen-bond with only one of the two hydroxyls near the T_v -sites (Fig. 2e). In the talc-like 10 \AA phase (precisely $d_{\text{OOL}} = 10.5 \text{ \AA}$), however, as the upper and lower T_v -sites are staggered, each hydroxyl near the T_v -site forms a hydrogen-bond with interlayer H_2O (Fig. 2f). This configuration leads to two small peaks in the interlayer water density profile whereas the phlogopite-like 10 \AA phase displays a single broad feature in the interlayer water density (Fig. 2b). It would, however, be reasonable to assign a single layer (1W) hydration state for the 10 \AA phases as the interlayer water

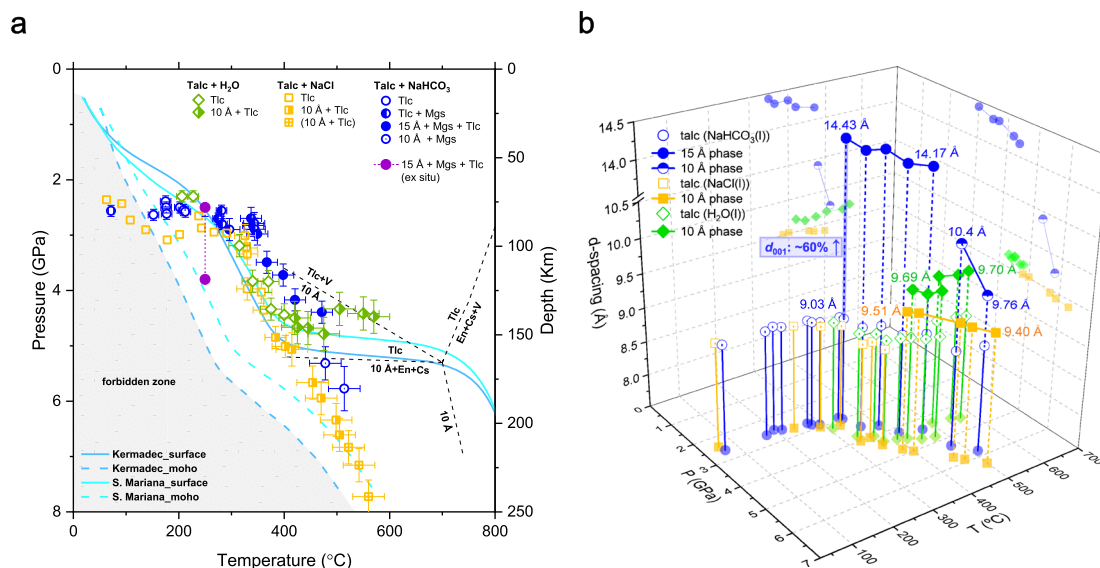


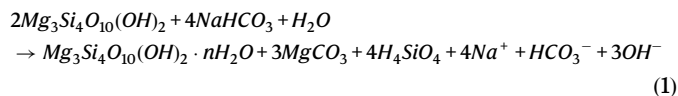
Fig. 1 | P-T stability and changes in the basal d-spacing of talc under modeled subduction fluid along cold subduction geotherms. a P-T stability of talc and its breakdown products under modeled subduction fluid along cold subduction geotherms. The error bars represent pressure and temperature uncertainties (see Supplementary Table S1). Continuous and dashed curves denote the P-T paths of subducting slab surfaces and corresponding slab Moho, respectively, of two different cold subduction thermal models from Syracuse et al.,⁵⁸. Black dashed lines

represent previously established stability fields of talc.^{29,30,83–85} **b** P-T dependent evolution of the basal d-spacing of talc under modeled subduction fluid along cold subduction geotherms. Each colored symbol represents talc under NaHCO₃ solution (blue circle, purple circle for ex-situ), NaCl solution (yellow square), and H₂O (green diamond). Phase abbreviations: Talc (Tlc), 10 Å phase (10 Å), super-hydrated 15 Å phase (15 Å), Enstatite (En), Magnesite (Mgs), Quartz (Qtz), Coesite (Cs) and Vapor/Fluid (V).

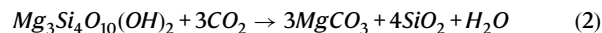
molecules themselves lack hydrogen-bonded networks with intermolecular distances of ~5 Å. The H₂O molecules bound to the hydroxyls near the *T_h*-sites were also identified in the 12 and 15 Å phases as small shoulder peaks in the water density profiles (Fig. 2g). Interlayer water molecules corresponding to the main peaks in the double-layer (2W) and tri-layer (3W) water densities of respective 12 and 15 Å phases are interconnected to form hydrogen-bonded networks with intermolecular distances of ~2.9 Å, featuring dynamic trajectories in their atomic positions. We suspect that the composition of fluid would affect further the formation and relative stabilities of the hydrated talc phases as our GCMC and MD simulations have not accounted for the effects of salts and/or alkalinity in the interlayer hydration.

In order to access the phase stability and evaluate the isothermal compressibility of the super-hydrated 15 Å phase, we have performed ex-situ HP-HT synchrotron XRD experiment under the same alkaline salty water condition using NaHCO₃ solution up to 7.0(1) GPa (Supplementary Table 3 and Supplementary Fig. 3). The formation of the 15 Å phase assemblage from talc was observed at 3.8(1) GPa after heat treatment to 250 °C at 2.5(1) GPa (Supplementary Fig. 3), which was recovered to ambient condition to show the *d*₀₀₁-spacing of ~15.22(1) Å for the uncompressed 15 Å phase (Supplementary Table 3). Isothermal compression at room temperature then showed gradual contraction of the *d*₀₀₁-spacing for the 15 Å phase up to 7.0(1) GPa, which gave rise to a calculated linear compressibility (along the *c*-axis or *d*₀₀₁-spacing) of $\beta = 4.16 \times 10^{-2}$ (GPa⁻¹) for the 15 Å phase (Supplementary Fig. 4 and Supplementary Table 4). This value is about three and two times larger than those of the original talc and its 10 Å phase, respectively (refs. 35,36), which demonstrates that the 15 Å phase is potentially, also paradoxically, one of the most compressible minerals that forms under subduction environments. After the ex-situ experiment, we treated the recovered 15 Å phase with ethylene glycol solvation (C₂H₆O₂) to examine its swelling property. As a result, the interlayer spacing has expanded to ~16.6 Å to confirm the smectite-like swelling feature of the super-hydrated 15 Å phase (Supplementary Fig. 5). Overall, the hydration reaction of talc under alkaline salty fluid condition along cold

subduction geotherm can be summarized as follows:



To evaluate the role of CO₂ in the Na₂O-CO₂-H₂O fluid system, additional ex-situ HP-HT synchrotron XRD experiment was performed using talc under pure CO₂ medium up to ~8 GPa and temperature treatment up to 300 °C. Unlike the hydration reaction observed in the Na₂O-CO₂-H₂O fluid system, the formation of the super-hydrated 15 Å phase has not been observed as talc decomposed to form magnesite and quartz assemblage near 1.7(1) GPa after heating to 260 °C (Supplementary Fig. 2d). The dehydration breakdown scheme of talc in pure CO₂ medium can be summarized as below:



Although most carbon-bearing geological fluids in the Earth's mantle (at temperatures above 400 °C) exist as the C-O-H system, including species such as H₂O, CO₂, CH₄, H₂, CO, O₂, and C₂H₆ (refs. 37,38), the reaction conditions (2) in our study would prefer the formation of magnesite (at temperatures below 400 °C), rather than the complex evolution of the fluid system itself. It has been known that magnesite is the major component of subducting carbonates to account for the carbon recycling through the deep mantle as its stability in the high pressure form extends to the lowermost mantle conditions, i.e., ~115 GPa and ~2100–2200 °C (ref. 39).

On the other hand, when NaCl solution or pure H₂O are used as pressure transmitting medium along the similar P-T path, talc transforms directly to the 10 Å phase, as observed in the previous studies^{31–33}, without transforming to the super-hydrated 15 Å phase assemblage (Fig. 1 and Supplementary Figs. 2b and 2c). The *d*₀₀₁-spacing of the 10 Å phase formed under NaCl solution medium appears to be modulated to 9.51(1) Å at 4.8(2) GPa and 385 ± 20 °C, compared to

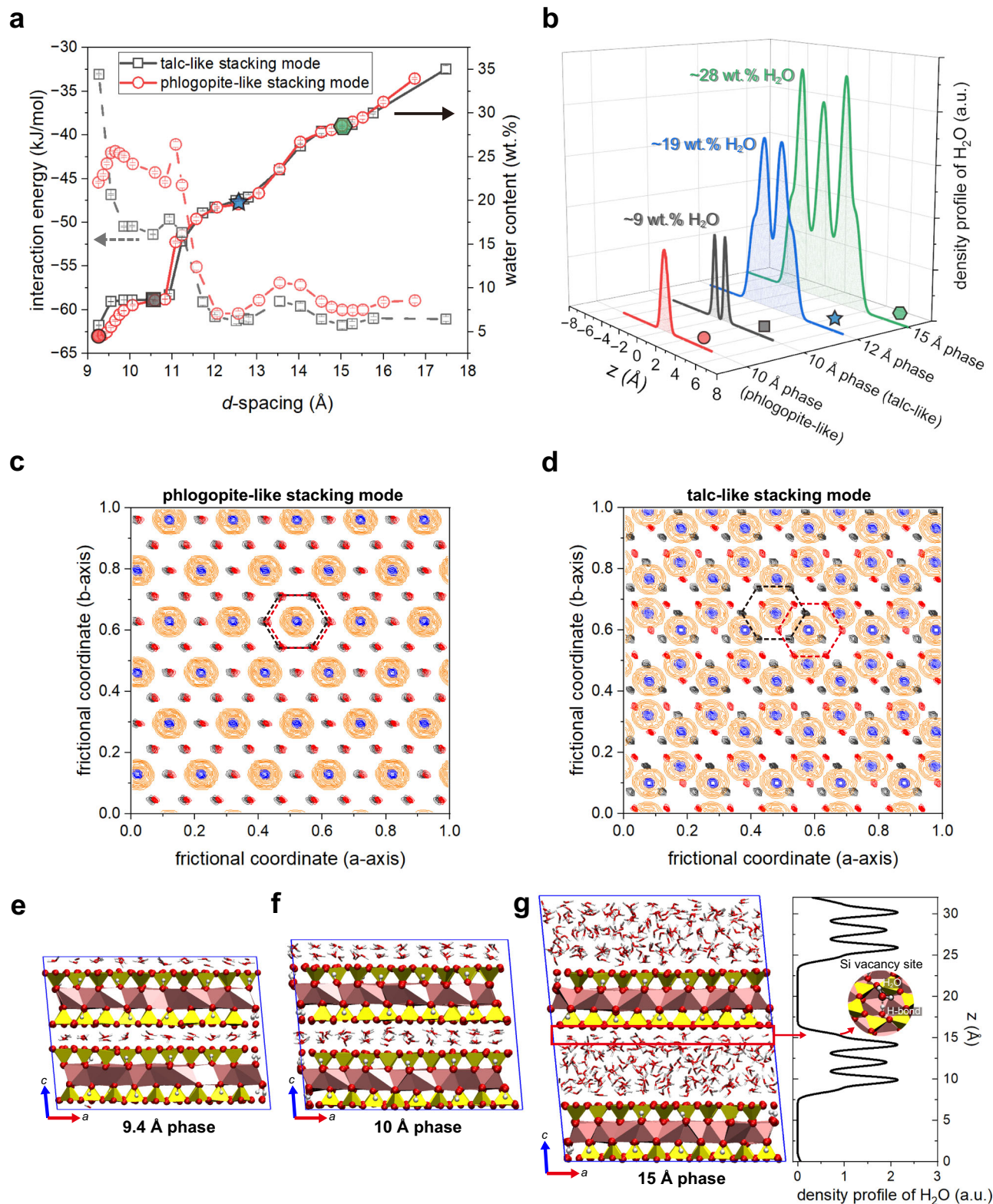
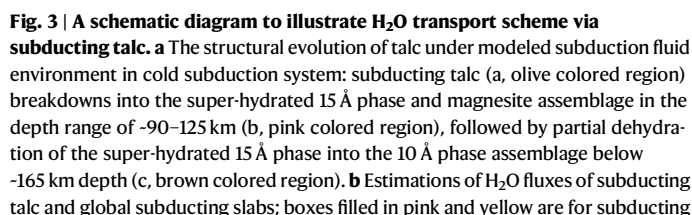


Fig. 2 | Grand canonical Monte Carlo (GCMC) and Molecular dynamics (MD) simulation results. a Interlayer water content and interaction energy of hydrated talc phases as a function of basal d-spacing for two different stacking modes.

b Density distribution of water (O atom) within the interlayer of 10, 12, and 15 Å phases of talc as calculated with NPT MD simulations (P = 3 GPa and T = 350 °C). **c, d** 2-D density distribution of H₂O molecules and basal oxygens of Si tetrahedral (T) layers in (c) phlogopite-like 10 Å phase and (d) talc-like 10 Å phase averaged over 10 ns of MD simulations. Dashed hexagons represent two Si vacancy sites (T_v-site)

of adjacent T-layers across the interlayer region. Black and red contours represent the basal oxygen positions of the adjacent T-layers. Blue and orange contours represent the O and H positions of water molecules, respectively. **e, f** and **g** MD simulation snapshots for each phase; (**e**) 9.4 Å phase, (**f**) 10 Å phase, and (**g**) super-hydrated 15 Å phase with density profile of its interlayer water (O atom) across the z-direction. Red rectangle and arrows indicate water bound to the vertically-oriented hydroxyls near the T_v-site via H-bonds. In the snapshot, yellow = Si tetrahedra, pink = Mg octahedra, red = O atoms, white = H atoms.



talc in cold and warm subduction zones, respectively, while boxes filled in navy are for global subducting slabs (based on the literature as summarized in Table 1). The boxes filled in light pink by dotted lines are enhanced estimations in the H_2O fluxes to account the super-hydration and subsequent partial dehydration via the 15 Å phase (see Table 1 for the volatiles budget estimations). Depth ranges for subducting slab are shown in parenthesis. **c** H_2O transport capacity of subducting talc compared to global subducting slabs by depths.

With regards to the source of water for the formation of the super-hydrated 15 Å phase in subduction environments, diverse cases of fluid generation, flow paths, and even local concentrations need to be assumed. One of the relevant processes is a dewatering in subduction zones that causes significant discharge of water into the overlying mantle^{45,46}. Much of this fluid, however, is likely released at relatively shallow depths, escaping toward the surface. It has also been generally assumed that fluids migrate into the mantle wedge due to the vertically decreasing pressure. On the other hand, there are other perspectives on the migration pathways of subduction fluids, with potential deep fluid flow including upward migration, entrapment within the slab, updip migration along the slab, or even downward flow into deeper parts of the subducting slab^{47–52}. For examples, hydrous fluids can

Table 1 | Estimated global H₂O flux by subducting talc based on the observed super-hydration processes in the cold subduction zones

Parameters	Value	References
thickness of oceanic crust	5–8 km	Geissler et al. and White et al. ^{78,79}
sediment (layer 1)	0.4–0.9 km	Straume et al. and references therein ⁸⁰
basalt (layer 2 A, B)	1.5–2.1 km	Vine et al. and White et al. ^{78,81}
gabbro with layered peridotite (layer 3)	4.5–5.0 km	Vine et al. and White et al. ^{78,81}
volume of oceanic crust	113–337 × 10 ⁶ km ³	Straume et al. and references therein ⁸⁰
sediment (layer 1)	2100 × 10 ⁶ km ³	Wyllie ⁸²
basalt (layer 2 A, B)		
gabbro with layered peridotite (layer 3)		
volume of talc in the subducting slab	–5.65–67.4 × 10 ⁶ km ³	Schmidt & Poli ¹
in layer 1 (~5–20 vol.%)	< –30 × 10 ⁶ km ³	*volumetric ratio of layer 2: layer 3 = 2:5
in layer 2 (<5 vol. %)	~75–300 × 10 ⁶ km ³	
in layer 3 (~5–20 vol. %)		
mass of talc in the subducting slab	–1.6–19 × 10 ²² g	*density of talc: –2.78 g/cm ³ (Gleason et al.,) ³⁵
in layer 1	< –8.3 × 10 ²² g	
in layer 2	–21–83 × 10 ²² g	
in layer 3		
amount of H ₂ O by subducting talc and its hydration products in cold subduction zones	–0.42–1.5 × 10 ²² g	Estimated from this study:
subducting talc	(av. –0.96 × 10 ²² g)	talc, Mg ₃ Si ₄ O ₁₀ (OH) ₂
15 Å phase	–0.36–1.3 × 10 ²³ g	15 Å phase, Mg ₃ Si ₄ O ₁₀ (OH) ₂ ·nH ₂ O (n = 8)
10 Å phase	(av. –8.3 × 10 ²² g)	10 Å phase, Mg ₃ Si ₄ O ₁₀ (OH) ₂ ·nH ₂ O (n = 2)
	–1.2–4.5 × 10 ²² g	
	(av. –2.9 × 10 ²² g)	
H ₂ O flux by subducting talc and its hydration products in cold subduction zones	–0.21–0.75 × 10 ¹⁴ g/yr	Estimated from this study:
subducting talc	(av. –0.48 × 10 ¹⁴ g/yr)	*assuming the cycle of oceanic crust to be 200 Ma
15 Å phase	–1.8–6.5 × 10 ¹⁴ g/yr	*assuming the cold subduction zones in global
10 Å phase	(av. –4.2 × 10 ¹⁴ g/yr)	subduction system to be ~28.5%
	–0.62–2.2 × 10 ¹⁴ g/yr	
	(av. –1.4 × 10 ¹⁴ g/yr)	

originate from the dehydration of serpentinized lithosphere at depths between 120–200 km, migrating upward through the overlying mantle⁴⁷. Some aqueous fluids may remain trapped within the subducting slab as free fluid or interstitial components, transported deeper into the mantle to depths beyond ~150 km^{48–50}. Additionally, part of the released water could migrate updip along the slab⁵¹. Meanwhile, stress changes due to the bending of the oceanic plate could induce subhydrostatic or negative pressure gradients along normal faults, promoting downward fluid flow within the slab⁵². Therefore, we might infer that the released fluid does not simply disappear in the slab system; instead, it can be retained and redistributed through various processes within the system.

In modern subduction system, the H₂O flux originating from hydrous minerals in the subducting slab has been estimated to be in the range of $-2.8 - 5.4 \times 10^{14}$ g/yr (av. -4.1×10^{14} g/yr) in a depth range of 100–150 km, which decreases to $-2.2 - 3.4 \times 10^{14}$ g/yr (av. -2.8×10^{14} g/yr) in a deeper region of 150–230 km as a result of (partial) dehydration⁴ (Fig. 3b). Based on the estimated amount of talc in the oceanic crust, i.e., <5–20 vol %, the initial H₂O flux contributed through talc can be estimated to be $-0.73 - 2.6 \times 10^{14}$ g/yr (av. -1.7×10^{14} g/yr) (Fig. 3b, Table 1 and references therein). By assuming that in cold subduction zones, the subducting talc undergoes super-hydration to the 15 Å phase as observed in this study, we can re-evaluate the H₂O flux of subducting slab down to ~300 km depth. From the depth of ~90 km, the water contents transported by talc would increase via the formation of the 15 Å phase by ~770% (ca. 8 folds) from $-0.42 - 1.5 \times 10^{22}$ g H₂O to $-0.36 - 1.3 \times 10^{23}$ g H₂O, i.e., from av. -0.48×10^{14} g H₂O/yr to -4.2×10^{14} g H₂O/yr (Fig. 3b and Table 1). This requires reevaluation of the H₂O flux by global subducting slabs from av. -4.1×10^{14} g H₂O/yr to -7.8×10^{14} g H₂O/yr in the intermediate depth range of ~90–150 km, which leads to an increase in the H₂O transport capacity of subducting talc from ~5.6% to ~53.5% (Fig. 3c). Such an estimated amount of the H₂O uptake is $-0.32 - 1.2 \times 10^{23}$ g, which may be translated to ~85–310 m of sea level reduction (or ~2.3–8.3% of global ocean) over 200 Ma (Table 1). While the super-hydrated 15 Å

phase remains stable down to ~125 km depth, the partial dehydration from the 15 Å to 10 Å phase would occur in the depths below ~165 km to release $-2.4 - 8.6 \times 10^{22}$ g of H₂O to the surrounding mantle, which is equivalent to $-1.2 - 4.3 \times 10^{14}$ g H₂O/yr (or ~1.7–6.1% of global ocean) over 200 Ma (Table 1).

The H₂O transportation along subduction zones affects arc magmatism and earthquakes^{51,53}. Specifically, arc magma generation is controlled by the dehydration reactions of subducting hydrous minerals^{34,55}, which is in turn influenced by subduction-related factors such as slab age, convergence rate, and slab dip⁵⁶, together with other thermal characteristics of the subduction zone⁵⁷. In order to find any correlations between the stability of subducting talc-related phases and subduction volcanism and seismicity, we have compiled the depths to the top of the slab beneath volcano (*H*) using volcano-specific subduction parameters of the global arc system at 298 volcanic centers above cold subductions (data from Syracuse and Abers, ref. 58). As a result, ~25% of volcanoes located above 15 cold subduction zones have *H* values within the range from 125 to 175 km (Fig. 4a). More specifically, for volcanoes above the South Mariana subduction zones, for which we modeled the P–T path of subducting talc, the *H* value is estimated to be ~134 km, for which the corrected *H* values (*H*_{corr}) become ~156 km (Fig. 4a) after accounting for hypocenter errors. In this study, we showed that super-hydration of subducting talc would occur in the depth range of ~90–125 km while the partial dehydration of the super-hydrated 15 Å phase to the 10 Å phase would occur near ~165 km. Given the apparent correlation between the corrected slab depths beneath arc volcanoes and our experimental results, we speculate that the dehydration of the super-hydrated 15 Å phase may partially be contributing to the arc magma generation.

Furthermore, intermediate-depth seismicity in subduction zones is known to be induced by mechanisms such as dehydration embrittlement⁵⁹, phase transformation⁶⁰, hydration⁶¹, stress transfer⁶², and thermal runaway instabilities⁶³. To find correlations of our observations to the seismicity of subduction zones, we have plotted the distribution of seismic frequencies along the South Mariana subduction

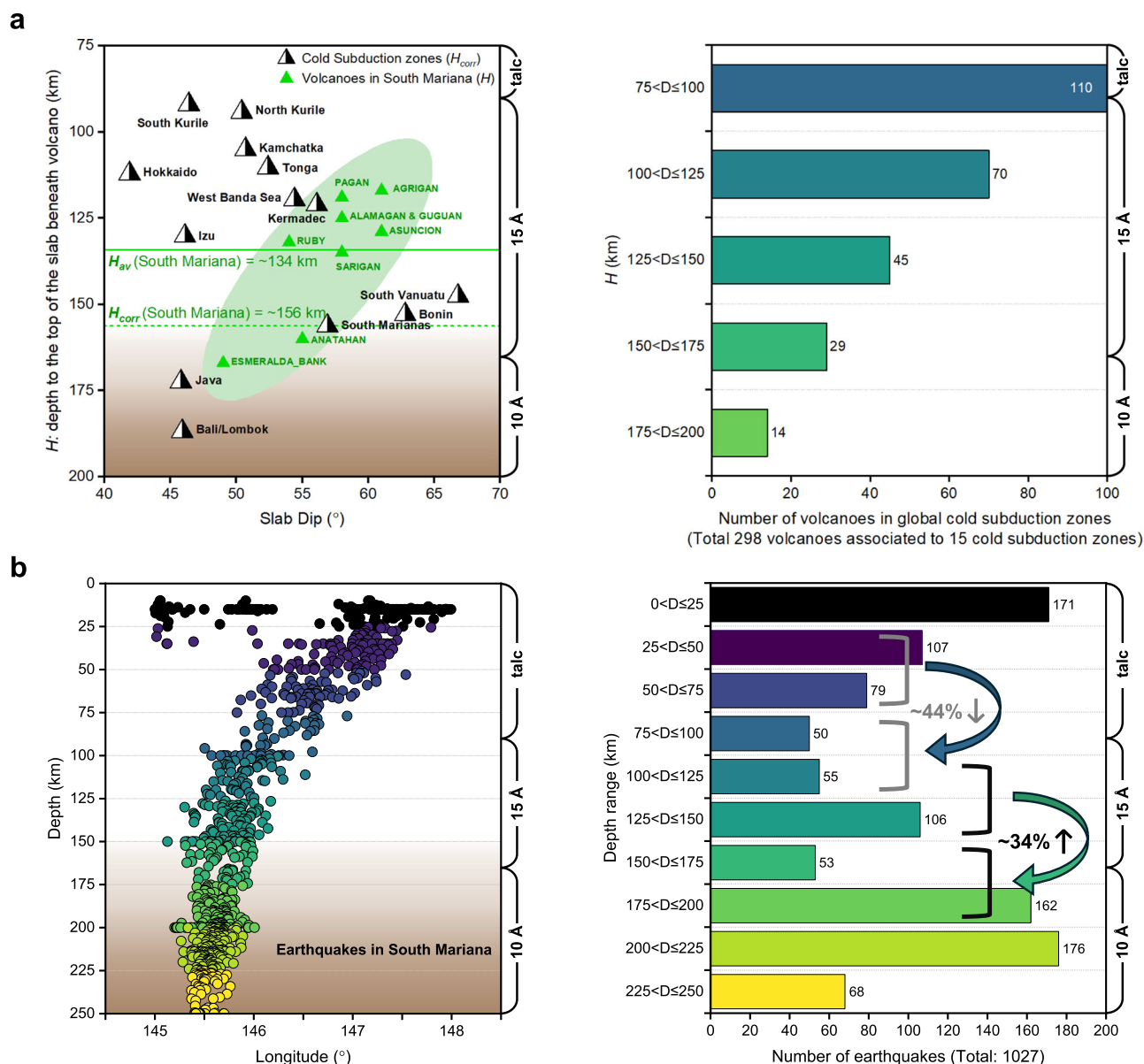


Fig. 4 | Correlation between the stability of subducting talc and subduction-related volcanism and seismicity. a Volcanoes in the South Mariana and other cold subduction systems using volcano-specific subduction parameters of the global arc system at 298 volcanic centers (data from Syracuse and Abers (2006)). The number of volcanoes along 15 cold subduction zones is shown by H (depths to the

top of the slab beneath volcano) intervals of ~25 km in the right panel. **b** Earthquake distribution in the South Mariana subduction systems over the past 20 years using data from the International Seismological Center (2024), ISC-EHB dataset^{86–88}. The depth-dependent earthquake frequency (in intervals of ~25 km) is shown in the right panel.

zones (Fig. 4b). We find that the earthquake frequencies *decrease* by ~44% in the depth range of 75–125 km, which overlaps with the formation depth of the super-hydrated 15 Å phase (~90–125 km). On the other hand, the earthquake frequencies *increase* by ~34% in the depth range of 150–200 km, which appears to be correlated to the partial dehydration depth of the super-hydrated 15 Å phase (~165 km depth).

In summary, we have found a mineral breakdown reaction that facilitates water transport into the Earth's interior. By taking into account the chemical and thermal characteristics of contemporary subduction system, the efficiency of water transport can be significantly revised to be enhanced via the formation of the super-hydrated 15 Å phase where carbonation reaction co-operates. Considerations on such complex nature of mineral-fluid interactions under realistic subduction environments are necessary to deepen our understanding of subduction-related volcanism and seismicity as well as volatile transport and cycling into the Earth's interior.

Methods

Sample and initial characterization

Initial characterization of talc (The Smithsonian Institution, NMNH B17990/ IGSN NHB0027G4, Falkenköpfle, Zillertal Valley, Tirol, Austria) used in this study was performed using X-ray diffraction (XRD) and field emission scanning electron microscope (FE-SEM, JEOL-7800F) equipped with energy-dispersive spectrometer (EDS, Oxford Instruments) (Supplementary Fig. 1). The chemical composition and morphology on talc were identified by using scanning electron microscopy (SEM) and energy dispersive spectroscopy (EDS). SEM images of talc show layered morphology while the calculated chemical formula from semi-quantified EDS results is derived to be $(\text{Mg}_{3-x}\text{Fe}_x)\text{Si}_4\text{O}_{10}(\text{OH})_2$ with $x < 0.05$. The XRD pattern on talc was indexed as space group C-1 with refined cell parameters of $a = 5.3172(9)$ Å, $b = 9.1666(6)$ Å, $c = 9.4890(15)$ Å, $\alpha = 90.779(11)^\circ$, $\beta = 99.064(14)^\circ$, $\gamma = 89.923(8)^\circ$.

We have performed ex-situ and in-situ high-pressure and high-temperature synchrotron X-ray diffraction experiments to investigate the stability of talc in the $\text{Na}_2\text{O}-\text{CO}_2-\text{NaCl}-\text{H}_2\text{O}$ system using sodium bicarbonate (NaHCO_3 , 0.5 M, pH -8.3) and sodium chloride (NaCl , 0.5 M) solutions as pressure-transmitting fluid (PTM).

Ex-situ high-pressure and high-temperature synchrotron x-ray powder diffraction

Ex-situ synchrotron X-ray powder diffraction measurements on talc under NaHCO_3 and CO_2 medium were performed using symmetric diamond anvil cell (DAC) at beamline 6D UNIST-PAL of Pohang Light Source-II (PLS-II) and at beamline BL10-2 of Stanford Synchrotron Radiation Lightsource (SSRL), respectively. At beamline 6D, the X-ray beam from the bending magnet was tuned to a wavelength of 0.653 Å (18.986 keV) and a beam size of $200 \times 200 \mu\text{m}^2$. A 2D CCD detector (MX225-HS, Rayonix L.L.C., USA) was used to collect diffraction data at -231 mm from the sample using 100 sec exposure time. At beamline BL10-2, the X-ray beam from the wiggler was tuned to a wavelength of 0.61992 Å (20.0 keV) and a beam size of $100 \times 100 \mu\text{m}^2$. A Pilatus 300K-w Si-diode CMOW detector was used to collect diffraction data at -1114 mm from the sample to cover 2-theta range of up to 30° for 200 sec exposure time. A symmetric-type DAC with culet diameter of 500 μm was used as a high-pressure vessel. A stainless-steel gasket of 250 μm in thickness was indented to ca. 80 μm , and a hole of ca. 250 μm in diameter was drilled in the center as a sample chamber using an electric discharge machine. For NaHCO_3 medium run, the powdered talc sample was loaded with sodium bicarbonate solution (NaHCO_3 , 0.5 M, pH -8.3) into the gasket hole with a few ruby spheres of several microns in size as pressure marker. The sample was then pressurized up to -7 GPa while the temperature was applied ex-situ by placing the DAC in a furnace at ca. 250 $^\circ\text{C}$ for 24 h. For CO_2 PTM run, the powdered talc sample was loaded with CO_2 under liquid-nitrogen cooled condition into the gasket hole with a few ruby spheres as pressure marker. The sample was then compressed up to -5 GPa while the temperature was applied ex-situ by placing the DAC in a furnace at ca. 260 $^\circ\text{C}$ for 2 h.

In-situ high-pressure and high-temperature synchrotron x-ray powder diffraction

In-situ synchrotron X-ray powder diffraction measurements were performed at 3D-XRS beamline at PLS-II, South Korea, 13-BMC beamline at Advanced Photon Source (APS), USA, and the Extreme Conditions Beamline (ECB) P02.2 at PETRA-III, Germany, as previously described in Hwang et al.²³. At beamline 3D, the X-ray beam from the bending magnet was tuned to a wavelength of 0.6888(1) Å (18.0 keV) or 0.6877(1) Å (18.03 keV) and beam size of $100 \times 100 \mu\text{m}^2$. A Mar345 image plate detector was used to collect diffraction data at a distance of 315.7 mm from the sample with 200 sec exposure time. At beamline 13-BMC, the X-ray beam from the bending magnet source was tuned to a wavelength of 0.4340(1) Å (28.568 keV) and focused to $12 \times 18 \mu\text{m}^2$ in size (FWHM) using a KB-mirror. A PILATUS 1M detector was used to collect diffraction data at distance of -169 mm from the sample with 150 sec of exposure time. At beamline P02.2, the X-ray beam from the undulator source was tuned to a wavelength of 0.4845(1) Å (25.590 keV) and focused to $8 \times 4 \mu\text{m}^2$ in size (FWHM) using Compound Refractive Lense (CRL) optics. A Perkin Elmer XRD 1621 detector was used to collect diffraction data at distance of -404 mm from the sample with 10 sec of exposure time. As a pressure vessel, symmetric-type DAC with culet diameter of 500 μm was used. A stainless-steel gasket of 250 μm in thickness was indented to ca. 40–60 μm , and a hole of ca. 250 μm in diameter was drilled in the center as a sample chamber using an electric discharge machine. Simultaneous P-T condition was created by the combination of a membrane device for online pressure control and a resistive electrical heater (a coil heater (at PLS and APS) and a graphite foil heater (at PETRA-III)) surrounding the diamond anvils. The coil heater was made of a kanthal (iron-chromium-

aluminum alloys) wire of 0.45 mm in diameter with 2.2 Ω resistance. The graphite foil heater was made of a flexible graphite sheet of 0.5 mm in thickness with -0.3 Ω resistance (A more detailed description of graphite RH-DAC setup can be found in the literature⁶⁴). Temperature was monitored using a K-type or a R-type thermocouple attached to the pavilion of the diamond anvil close to the sample, which allowed the maximum uncertainties of $\pm 30^\circ\text{C}$. Pressure was calculated using the equation of state of Au or Cu pressure marker^{65,66} included in the sample chamber. Initially, we compressed the sample to -1.0–2.0 GPa and then increased the pressure and temperature in increments of -0.5 GPa and 50 $^\circ\text{C}$ up to -7.7 GPa and -560 $^\circ\text{C}$, respectively (Supplementary Table 1).

Atomistic simulations of hydrated talc phases

Talc crystal structures were constructed by expansion of the experimental unit cell structure⁶⁷ to a $5 \times 3 \times 2$ supercell ($a = 26.30$ Å, $b = 27.30$ Å, $c = 18.81$ Å, $\alpha = \gamma = 90^\circ$, $\beta = 100^\circ$). For hydrated talc phases, H_2O molecules were inserted to the interlayer of the pure talc supercell in two forms of TOT layer stacking, i.e., talc-like and phlogopite-like stacking modes. The CLAYFF force field⁶⁸ was used to describe the interatomic potential of talc, and the SPC/E potential⁶⁹ was used for water molecules. The Lorentz-Berthelot combination rule was applied to the potential between heteroatoms⁷⁰. For evaluation of the maximum water contents of talc at given d -spacings, GCMC simulations were performed using the GIBBS code⁷¹. The chemical potential of the water reservoir corresponding to the state of 3 GPa and 350 $^\circ\text{C}$ was determined by the Widom insertion test of bulk water⁷². We performed an equilibrium run of 20 million MC steps and a production run of 100 million MC steps at the fixed chemical potential. Insertion or deletion of water molecules was attempted with a probability of 70%, translation with a probability of 15%, and rotation with a probability of 15%. The interaction energies between talc and intercalating water, calculated corresponding to the maximum water contents, are reported per water molecule. MD simulations were performed with NPT ensemble (350 $^\circ\text{C}$, 3 GPa) for hydrated talc phases based on the water contents determined by GCMC simulations. We used the LAMMPS code⁷³, with an equilibrium run for 1 ns and a production run for 10 ns. The temperature and pressure were controlled using Nosé-Hoover chain thermostats^{74,75}. For long-range electrostatics, Ewald summation with an accuracy of 0.0001 kcal/mol was applied⁷⁶. The SHAKE algorithm was used to maintain the rigidity of SPC/E water⁷⁷. Additional simulations were performed at 470 $^\circ\text{C}$ and 4.4 GPa, but no significant differences between the phases were observed.

Data availability

All the data generated in this study are available within the Article, Supplementary Information, or Source Data file. Source data is deposited in the figshare repository (<https://doi.org/10.6084/m9.figshare.27316125>). Any additional data are available from the corresponding author upon request.

Code availability

All data presented in this manuscript were obtained without the use of custom code.

References

- Schmidt, M. W. & Poli, S. 4.19 - Devolatilization During Subduction. *Treatise on Geochemistry (Second Edition)*, 669–701 (2014).
- Faccenda, M. Water in the slab: a trilogy. *Tectonophysics* **614**, 1–30 (2014).
- Ohtani, E. Water in the mantle. *Elements* **1**, 25–30 (2005).
- van Keken, P. E., Hacker, B. R., Syracuse, E. M. & Abers, G. A. Subduction factory 4. depth-dependent flux of H_2O from subducting slabs worldwide. *J. Geophys. Res. Solid Earth* **116**, B01401 (2011).

5. Grove, T. L., Chatterjee, N., Parman, S. W. & Médard, E. The influence of H₂O on mantle wedge melting. *Earth Planet. Sci. Lett.* **249**, 74–89 (2006).
6. Hacker, B. R. H₂O subduction beyond arcs. *Geochem. Geophys. Geosyst.* **9**, Q03001 (2008).
7. Korenaga, J. Urey ratio and the structure and evolution of Earth's mantle. *Rev. Geophys.* **46**, RG2007 (2008).
8. Ganne, J. & Feng, X. Primary magmas and mantle temperatures through time. *Geochem. Geophys. Geosyst.* **18**, 872–888 (2017).
9. Weller, M. B. & Lenardic, A. On the evolution of terrestrial planets: bi-stability, stochastic effects, and the non-uniqueness of tectonic states. *Geosci. Front.* **9**, 91–102 (2018).
10. Palin, R. M. et al. Secular change and the onset of plate tectonics on Earth. *Earth-Sci. Rev.* **207**, 103172 (2020).
11. Dolejš, D. & Wagner, T. Thermodynamic modeling of non-ideal mineral–fluid equilibria in the system Si–Al–Fe–Mg–Ca–Na–K–H–O–Cl at elevated temperatures and pressures: Implications for hydro-thermal mass transfer in granitic rocks. *Geochim. Cosmochim. Acta* **72**, 526–553 (2008).
12. Manning, C. E. & Frezzotti, M. L. Subduction-zone fluids. *Elements* **16**, 395–400 (2020).
13. Keppler, H. Fluids and trace element transport in subduction zones. *Am. Mineral.* **102**, 5–20 (2017).
14. Frezzotti, M. L. & Ferrando, S. The chemical behavior of fluids released during deep subduction based on fluid inclusions. *Am. Mineral.* **100**, 352–377 (2015).
15. Holland, G. & Ballentine, C. J. Seawater subduction controls the heavy noble gas composition of the mantle. *Nature* **441**, 186–191 (2006).
16. Marion, G. M. et al. pH of seawater. *Mar. Chem.* **126**, 89–96 (2011).
17. Middelburg, J. J., Soetaert, K. & Hagens, M. Ocean alkalinity, buffering and biogeochemical processes. *Rev. Geophys.* **58**, e2019RG000681 (2020).
18. De Hoog, J. C. M. & Savov, I. P. *Boron Isotopes as a Tracer of Subduction Zone Processes*. (ed Marshall, H., Foster, G.) in *Boron Isotopes: The Fifth Element*. 217–247 (Springer International Publishing: Cham, 2018).
19. Mottl, M. J., Wheat, C. G., Fryer, P., Gharib, J. & Martin, J. B. Chemistry of springs across the Mariana forearc shows progressive devolatilization of the subducting plate. *Geochim. Cosmochim. Acta* **68**, 4915–4933 (2004).
20. Galvez, M. E., Connolly, J. A. D. & Manning, C. E. Implications for metal and volatile cycles from the pH of subduction zone fluids. *Nature* **539**, 420 (2016).
21. Mikhail, S., Barry, P. H. & Sverjensky, D. A. The relationship between mantle pH and the deep nitrogen cycle. *Geochim. Cosmochim. Acta* **209**, 149–160 (2017).
22. Li, H.-Y. et al. Molybdenum isotopes unmask slab dehydration and melting beneath the Mariana arc. *Nat. Commun.* **12**, 6015 (2021).
23. Hwang, G. C. et al. A role for subducted albite in the water cycle and alkalinity of subduction fluids. *Nat. Commun.* **12**, 1155 (2021).
24. Fumagalli, P., Stixrude, L., Poli, S. & Snyder, D. The 10 Å phase: a high-pressure expandable sheet silicate stable during subduction of hydrated lithosphere. *Earth Planet. Sci. Lett.* **186**, 125–141 (2001).
25. Ohtani, E., Litasov, K., Hosoya, T., Kubo, T. & Kondo, T. Water transport into the deep mantle and formation of a hydrous transition zone. *Phys. Earth Planet. Inter.* **143–144**, 255–269 (2004).
26. Ulmer, P. & Trommsdorff, V. Phase relations of hydrous mantle subducting to 300 km. In *Mantle petrology: Field observations and high pressure experimentation*. *Geochem. Soc. Spec. Publ.* **6**, 259–281 (1999).
27. Liou, J. G. & Zhang, R. Y. Significance of ultrahigh-P talc-bearing eclogitic assemblages. *Mineralogical Mag.* **59**, 93–102 (1995).
28. Chopin, C. Talc-Phengite: a widespread assemblage in high-grade pelitic blueschists of the western alps. *J. Petrol.* **22**, 628–650 (1981).
29. Chinnery, N. J., Pawley, A. R. & Clark, S. M. In situ observation of the formation of 10 Å phase from Talc + H₂O at mantle pressures and temperatures. *Science* **286**, 940–942 (1999).
30. Pawley, A. R. & Wood, B. J. The high-pressure stability of talc and 10 Å phase: potential storage sites for H₂O in subduction zones. *Am. Mineral.* **80**, 998–1003; (1995).
31. Yamamoto, K. & Akimoto, S. The system MgO–SiO₂–H₂O at high pressures and temperatures; stability field for hydroxyl-chondrodite, hydroxyl-clinohumite and 10 Å o-phase. *Am. J. Sci.* **277**, 288–312 (1977).
32. Wunder, B. & Schreyer, W. Metastability of the 10-Å phase in the system MgO–SiO₂–H₂O (MSH). what about hydrous MSH phases in subduction zones? *J. Petrol.* **33**, 877–889 (1992).
33. Bauer, J. F. & Sclar, C. B. The “10 Å phase” in the system MgO–SiO₂–H₂O. *Am. Mineral.* **66**, 576–585 (1981).
34. Comodi, P., Fumagalli, P., Nazzareni, S. & Zanazzi, P. F. The 10 Å phase: crystal structure from single-crystal X-ray data. *Am. Mineral.* **90**, 1012–1016 (2005).
35. Gleason, A. E., Parry, S. A., Pawley, A. R., Jeanloz, R. & Clark, S. M. Pressure-temperature studies of talc plus water using X-ray diffraction. *Am. Mineral.* **93**, 1043–1050 (2008).
36. Comodi, P., Cera, F., Dubrovinsky, L. & Nazzareni, S. The high-pressure behaviour of the 10 Å phase: a spectroscopic and diffractometric study up to 42 GPa. *Earth Planet. Sci. Lett.* **246**, 444–457 (2006).
37. Huizenga, J.-M. Thermodynamic modelling of C–O–H fluids. *Lithos* **55**, 101–114 (2001).
38. Zhang, C. & Duan, Z. A model for C–O–H fluid in the Earth's mantle. *Geochim. Cosmochim. Acta* **73**, 2089–2102 (2009).
39. Isshiki, M. et al. Stability of magnesite and its high-pressure form in the lowermost mantle. *Nature* **427**, 60 (2004).
40. Suquet, H., de la Calle, C. & Pezerat, H. Swelling and structural organization of saponite. *Clays Clay Min.* **23**, 1–9 (1975).
41. Colton-Bradley, V. Role of pressure in smectite dehydration—effects on geopressure and smectite-to-illite transition. *AAPG Bull.* **71**, 1414–1427 (1987).
42. Hüpers, A. & Kopf, A. J. Effect of smectite dehydration on pore water geochemistry in the shallow subduction zone: An experimental approach. *Geochem. Geophys. Geosyst.* **13**, <https://doi.org/10.1029/2012GC004212> (2012).
43. Pawley, A. R., Chinnery, N. J., Clark, S. M. & Walter, M. J. Experimental study of the dehydration of 10-Å phase, with implications for its H₂O content and stability in subducted lithosphere. *Contrib. Mineral. Petrol.* **162**, 1279–1289 (2011).
44. Rashchenko, S. V., Kamada, S., Hirao, N., Litasov, K. D. & Ohtani, E. In situ X-ray observation of 10 Å phase stability at high pressure. *Am. Mineral.* **101**, 2564–2569 (2016).
45. Peacock, S. M. Fluid processes in subduction zones. *Science* **248**, 329–338 (1990).
46. Bebout, G. E. & Barton, M. D. Metasomatism during subduction: products and possible paths in the Catalina Schist. *Calif. Chem. Geol.* **108**, 61–92 (1993).
47. Ulmer, P. & Trommsdorff, V. Serpentine stability to mantle depths and subduction-related magmatism. *Science* **268**, 858 (1995).
48. Bruce Watson, E. & Lupulescu, A. Aqueous fluid connectivity and chemical transport in clinopyroxene-rich rocks. *Earth Planet. Sci. Lett.* **117**, 279–294 (1993).
49. Mibe, K., Yoshino, T., Ono, S., Yasuda, A. & Fujii, T. Connectivity of aqueous fluid in eclogite and its implications for fluid migration in the Earth's interior. *J. Geophys. Res. Solid Earth* **108**, 2295 (2003).
50. Scambelluri, M. & Philippot, P. Deep fluids in subduction zones. *Lithos* **55**, 213–227 (2001).
51. Hacker, B. R., Peacock, S. M., Abers, G. A. & Holloway, S. D. Subduction factory 2. Are intermediate-depth earthquakes in

- subducting slabs linked to metamorphic dehydration reactions? *J. Geophys. Res. Solid Earth* **108**, 2030 (2003).
52. Faccenda, M., Gerya, T. V. & Burlini, L. Deep slab hydration induced by bending-related variations in tectonic pressure. *Nat. Geosci.* **2**, 790–793 (2009).
 53. Grove, T. L., Till, C. B. & Krawczynski, M. J. The role of H₂O in subduction zone magmatism. *Annu. Rev. Earth. Pl. Sc.* **40**, 413–439 (2012).
 54. Tatsumi, Y. Formation of the volcanic front in subduction zones. *Geophys. Res. Lett.* **13**, 717–720 (1986).
 55. Kerrick, D. M. & Connolly, J. A. D. Metamorphic devolatilization of subducted oceanic metabasalts: implications for seismicity, arc magmatism and volatile recycling. *Earth Planet. Sci. Lett.* **189**, 19–29 (2001).
 56. England, P., Engdahl, R. & Thatcher, W. Systematic variation in the depths of slabs beneath arc volcanoes. *Geophys. J. Int.* **156**, 377–408 (2004).
 57. England, P. & Wilkins, C. A simple analytical approximation to the temperature structure in subduction zones. *Geophys. J. Int.* **159**, 1138–1154 (2004).
 58. Syracuse, E. M. & Abers, G. A. Global compilation of variations in slab depth beneath arc volcanoes and implications. *Geochem. Geophys. Geosyst.* **7**, n/a–n/a (2006).
 59. Jung, H., Green, H. W. II & Dobrzynetska, L. F. Intermediate-depth earthquake faulting by dehydration embrittlement with negative volume change. *Nature* **428**, 545–549 (2004).
 60. Green, H. W. II, Shi, F., Bozhilov, K., Xia, G. & Reches, Z. Phase transformation and nanometric flow cause extreme weakening during fault slip. *Nat. Geosci.* **8**, 484–489 (2015).
 61. Barcheck, C. G., Wiens, D. A., van Keken, P. E. & Hacker, B. R. The relationship of intermediate- and deep-focus seismicity to the hydration and dehydration of subducting slabs. *Earth Planet. Sci. Lett.* **349–350**, 153–160 (2012).
 62. Ferrand, T. P. et al. Dehydration-driven stress transfer triggers intermediate-depth earthquakes. *Nat. Commun.* **8**, 15247 (2017).
 63. Braeck, S. & Podladchikov, Y. Y. Spontaneous thermal runaway as an ultimate failure mechanism of materials. *Phys. Rev. Lett.* **98**, 095504 (2007).
 64. Hwang, H. et al. Graphite resistive heated diamond anvil cell for simultaneous high-pressure and high-temperature diffraction experiments. *Rev. Sci. Instrum.* **94**, 083903 (2023).
 65. Anderson, O. L., Isaak, D. G. & Yamamoto, S. Anharmonicity and the equation of state for gold. *J. Appl. Phys.* **65**, 1534–1543 (1989).
 66. Tsuchiya, T. First-principles prediction of the P–V–T equation of state of gold and the 660-km discontinuity in Earth’s mantle. *J. Geophys. Res. Solid Earth* **108**, 2462 (2003).
 67. Gruner, J. W. The crystal structures of talc and pyrophyllite. *Z. f. ür. Kristallographie - Crystalline Mater.* **88**, 412–419 (1934).
 68. Cygan, R. T., Liang, J.-J. & Kalinichev, A. G. Molecular models of hydroxide, oxyhydroxide, and clay phases and the development of a general force field. *J. Phys. Chem. B* **108**, 1255–1266 (2004).
 69. Berendsen, H. J. C., Grigera, J. R. & Straatsma, T. P. The missing term in effective pair potentials. *J. Phys. Chem.* **91**, 6269–6271 (1987).
 70. Halgren, T. A. The representation of van der Waals (vdW) interactions in molecular mechanics force fields: potential form, combination rules, and vdW parameters. *J. Am. Chem. Soc.* **114**, 7827–7843 (1992).
 71. Mackie, A. D., Tavittian, B., Boutin, A. & Fuchs, A. H. Vapour-liquid phase equilibria predictions of methane–alkane mixtures by Monte Carlo simulation. *Mol. Simul.* **19**, 1–15 (1997).
 72. Widom, B. Some topics in the theory of fluids. *J. Chem. Phys.* **39**, 2808–2812 (1963).
 73. Plimpton, S. Fast parallel algorithms for short-range molecular dynamics. *J. Computational Phys.* **117**, 1–19 (1995).
 74. Martyna, G. J., Tuckerman, M. E., Tobias, D. J. & Klein, M. L. Explicit reversible integrators for extended systems dynamics. *Mol. Phys.* **87**, 1117–1157 (1996).
 75. Shuichi, N. Constant temperature molecular dynamics methods. *Prog. Theor. Phys. Suppl.* **103**, 1–46 (1991).
 76. Karasawa, N. & Goddard, W. A. III Acceleration of convergence for lattice sums. *J. Phys. Chem.* **93**, 7320–7327 (1989).
 77. Ryckaert, J.-P., Ciccotti, G. & Berendsen, H. J. C. Numerical integration of the cartesian equations of motion of a system with constraints: molecular dynamics of n-alkanes. *J. Computational Phys.* **23**, 327–341 (1977).
 78. White, R. S., McKenzie, D. & O’Nions, R. K. Oceanic crustal thickness from seismic measurements and rare earth element inversions. *J. Geophys. Res. Solid Earth* **97**, 19683–19715 (1992).
 79. Geissler, W. H., Jokat, W., Jegen, M. & Baba, K. Thickness of the oceanic crust, the lithosphere, and the mantle transition zone in the vicinity of the Tristan da Cunha hot spot estimated from ocean-bottom and ocean-island seismometer receiver functions. *Tectonophysics* **716**, 33–51 (2017).
 80. Straume, E. O. et al. GlobSed: updated total sediment thickness in the world’s oceans. *Geochem. Geophys. Geosyst.* **20**, 1756–1772 (2019).
 81. Vine, F. J. & Moores, E. M. A Model for the Gross Structure, Petrology, and Magnetic Properties of Oceanic Crust. (ed Shagam, R. et al.) in *Studies in Earth and Space Sciences*, **132** (Geological Society of America, 1972).
 82. Wyllie, P. J. *The Dynamic Earth: textbook in geosciences*. 139–165 (John Wiley & Sons, Inc.: New York (1971).
 83. Johannes, W. An experimental investigation of the system MgO–SiO₂–H₂O–CO₂. *Am. J. Sci.* **267**, 1083–1104 (1969).
 84. Jenkins, D. M., Holland, T. J. B. & Clare, A. K. Experimental determination of the pressure-temperature stability field and thermochemical properties of synthetic tremolite. *Am. Mineral.* **76**, 458–469 (1991).
 85. Boyd, F. R. & England, J. L. The quartz-coesite transition. *J. Geophys. Res.* **65**, 749–756 (1960).
 86. Engdahl, E. R., van der Hilst, R. & Buland, R. Global teleseismic earthquake relocation with improved travel times and procedures for depth determination. *Bull. Seismological Soc. Am.* **88**, 722–743 (1998).
 87. Weston, J., Engdahl, E. R., Harris, J., Di Giacomo, D. & Storchak, D. A. ISC-EHB: reconstruction of a robust earthquake data set. *Geophys. J. Int.* **214**, 474–484 (2018).
 88. Engdahl, E. R. et al. ISC-EHB 1964–2016, an improved data set for studies of earth structure and global seismicity. *Earth Space Sci.* **7**, e2019EA000897 (2020).

Acknowledgements

This work was supported by the Leader Researcher program of the Korean Ministry of Science and ICT (NRF-2018R1A3B1052042). Y.B. acknowledges the support by the Institute for Korea Spent Nuclear Fuel (iKSNF) and National Research Foundation of Korea (NRF) grant funded by the Korea government (Ministry of Science and ICT, MSIT) (No.2021M2E1A1085186) for the work performed at KAERI. K.D.K. thanks the support by the Korean Ministry of Education (NRF-No.2019R1A6A1A03033167), and D.Z. acknowledges the support by the National Science Foundation (EAR-1634415 and EAR-1661511). Synchrotron experiments were performed at beamline BL10-2 at SSR, the beamlines 3D and 6D at PLS-II, PAL, beamline 13-BMC at APS, and beamline ECB P02.2 at PETRA-III at Deutsches Elektronen-Synchrotron (DESY, Hamburg, Germany), a member of the Helmholtz Association HGF. We also acknowledge the scientific exchange and support of the Center for Molecular Water Science (CMWS) at DESY.

Author contributions

Y.B. and Y.L. conceived and designed the research. Y.B. performed synchrotron experiments and data analysis with the help from J.C., H.S., D.Z., T.-Y.J., T.J.S., and H.-P.L. J.K. and K.D.K. performed atomistic simulations. Y.B., J.K., K.D.K., and Y.L. wrote the initial draft of the manuscript. Y.L. supervised the research and worked on the manuscript with all authors.

Competing interests

The authors declare no competing interests.

Additional information

Supplementary information The online version contains supplementary material available at <https://doi.org/10.1038/s41467-025-56672-6>.

Correspondence and requests for materials should be addressed to Yongjae Lee.

Peer review information *Nature Communications* thanks Stefano Poli, and the other, anonymous, reviewer(s) for their contribution to the peer review of this work. A peer review file is available.

Reprints and permissions information is available at <http://www.nature.com/reprints>

Publisher's note Springer Nature remains neutral with regard to jurisdictional claims in published maps and institutional affiliations.

Open Access This article is licensed under a Creative Commons Attribution-NonCommercial-NoDerivatives 4.0 International License, which permits any non-commercial use, sharing, distribution and reproduction in any medium or format, as long as you give appropriate credit to the original author(s) and the source, provide a link to the Creative Commons licence, and indicate if you modified the licensed material. You do not have permission under this licence to share adapted material derived from this article or parts of it. The images or other third party material in this article are included in the article's Creative Commons licence, unless indicated otherwise in a credit line to the material. If material is not included in the article's Creative Commons licence and your intended use is not permitted by statutory regulation or exceeds the permitted use, you will need to obtain permission directly from the copyright holder. To view a copy of this licence, visit <http://creativecommons.org/licenses/by-nc-nd/4.0/>.

© The Author(s) 2025